

1 **Bimodal dendritic processing in basket cells drives distinct memory-related**
2 **oscillations.**

3 Alexandra Tzilivaki^{1,2,3 *}, Matthew Evan Larkum^{1,2,3,4}, Dietmar Schmitz^{1,2,3,5,6 * #}

4 ¹Charité-Universitätsmedizin Berlin, corporate member of Freie Universität Berlin, Humboldt-
5 Universität Berlin, and Berlin Institute of Health, Neuroscience Research Center, 10117
6 Berlin, Germany

7 ²Einstein Center for Neurosciences, Chariteplatz 1, 10117 Berlin, Germany

8 ³NeuroCure Cluster of Excellence, Chariteplatz 1, 10117 Berlin, Germany

9 ⁴Department of Biology, Humboldt Universität zu Berlin, Berlin 10117, Germany

10 ⁵German Center for Neurodegenerative Diseases (DZNE), 10117 Berlin, Germany

11 ⁶Bernstein Center for Computational Neuroscience, Humboldt-Universität zu Berlin,
12 Philippsstrasse. 13, 10115 Berlin, Germany

13 * Correspondence: dietmar.schmitz@charite.de, alexandra.tzilivaki@charite.de

14 # Main/Lead contact author

15

16 **Abstract**

17 Hippocampal oscillations span from slow to high-frequency bands that are linked to different
18 memory stages and behavioral states. We show that fast spiking basket cells (FSBCs) with
19 bimodal nonlinear dendritic trees modulate these oscillations. Supralinear FSBC dendritic
20 activation enhances high-frequency oscillations, while sublinear activation increases slow
21 oscillatory power, adjusting the Excitation/Inhibition balance in the network. This underscores
22 a new link between FSBCs nonlinear dendritic integration and memory-related oscillations.

23

24 **Main**

25 Hippocampal oscillations exhibit a variety of distinct frequency bands¹. For example,
26 neuronal activity often associates with a slow local field potential (LFP) component, known
27 as theta activity, which ranges from 3 to 10 Hz¹⁻³. Additionally, hippocampal activity includes
28 fast-frequency oscillations spanning from 30 to 200 Hz¹⁻⁵. Both experimental and
29 computational studies have linked these slow and fast components to different stages of
30 hippocampal memory formation and distinct behavioral states^{3,6,7}. Specifically, slow 3-10 Hz
31 oscillations correlate with memory encoding, spatial navigation, and sensory processing³.
32 Conversely, fast oscillations are associated with memory encoding and consolidation^{3,6}.
33 Notably, these fast and slow components often occur together in a phenomenon known as
34 oscillation coupling^{5,8-11} which has been proposed as a signature of working memory
35 processing and various behavioral states (**Fig.1a**)^{3,5}.

36 To understand the cellular mechanisms behind these oscillatory events, significant efforts
37 have been made to delineate the effects of various subclasses of both excitatory and
38 inhibitory hippocampal populations. Among these, PV+ GABAergic interneurons play a
39 crucial role in both slow and fast oscillations as well as in coupled oscillatory activity^{10,12-17}.
40 However, the vast majority of research has traditionally focused on the activation or silencing
41 of PV+ interneurons during oscillations through optogenetic and modeling approaches.

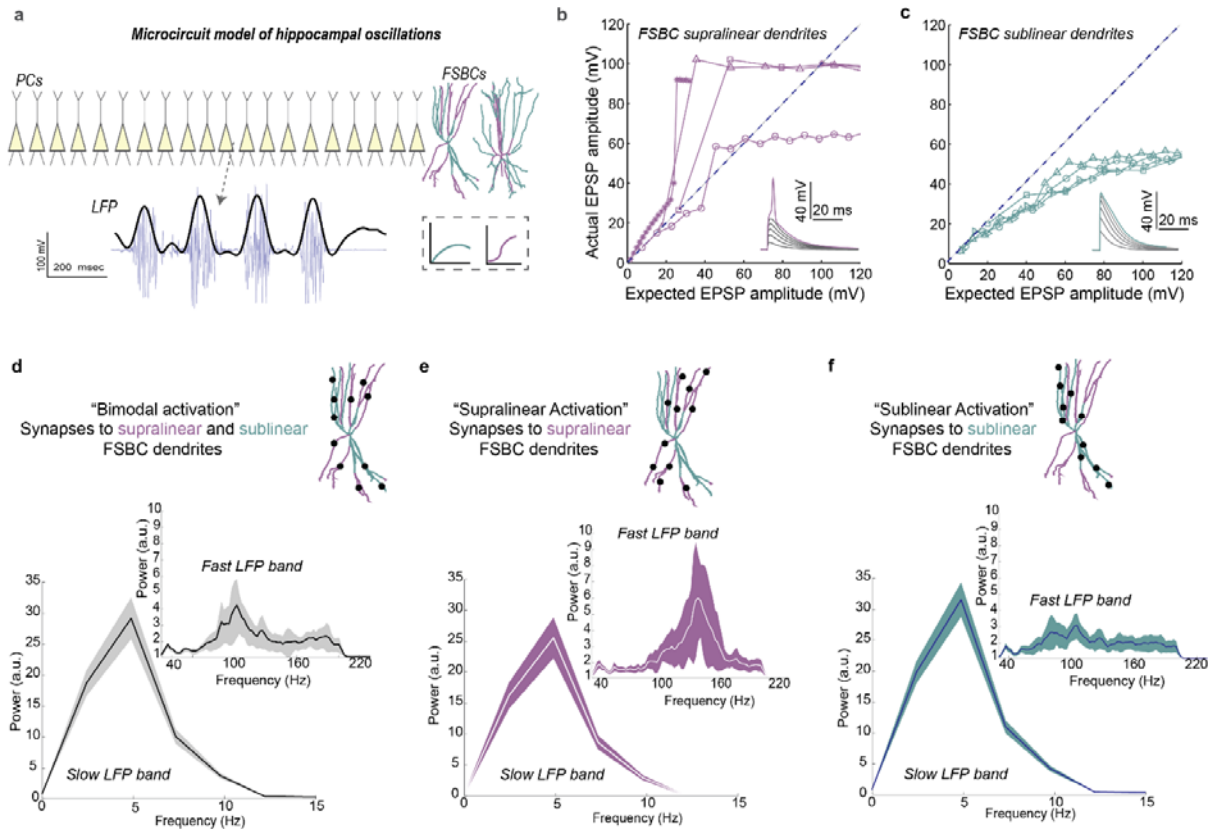
42 Recent computational and experimental studies reveal that PV+ interneurons exhibit diverse
43 nonlinear dendritic computations, significantly enhancing their computational capabilities and
44 shaping their input-output (I/O) configurations^{18–23}. Notably, a subtype of PV+ interneurons,
45 the Fast-Spiking Basket Cells (FSBCs), possesses bimodal nonlinear dendritic
46 integration^{18,19,24}. Specifically, multicompartmental biophysical modeling has shown that
47 FSBCs have two types of co-existing nonlinear dendrites: supralinear dendrites, which can
48 generate local dendritic spikes, and sublinear dendrites, which integrate excitatory synaptic
49 input passively (**Figs.1b-c,S1a-d**). While both types of nonlinear dendrites co-exist in the
50 same tree (**Fig.1b-c,S1**), and share similar active properties, they differ morphologically¹⁹.
51 Supralinear branches have higher volume, and lower input resistance, enabling local sodium
52 spikes (**Fig.S1a-e**). Conversely, sublinear branches have lower volume, and higher input
53 resistance. Thus, coincident synaptic input induces large, fast rising EPSPs that in turn
54 activate A-type potassium channels leading to a fast repolarization of the membrane, thus
55 preventing the generation of local sodium spikes (**Fig.S1a-d**). These modeling predictions¹⁹
56 are supported by recent experimental findings in PV+ interneurons across different
57 hippocampal areas^{18,20,21}.

58 However, it remains unknown whether the bimodal nonlinear nature of FSBCs dendrites
59 affects network function by modulating different memory-related oscillations. Given the
60 involvement of FSBCs in both slow (e.g. theta-frequencies) and fast oscillations^{12,25,26}, we
61 hypothesized that the supralinear or sublinear branches of FSBCs would differentially
62 modulate FSBCs activity and, consequently, their impact on orchestrating the LFP during
63 mnemonic functions.

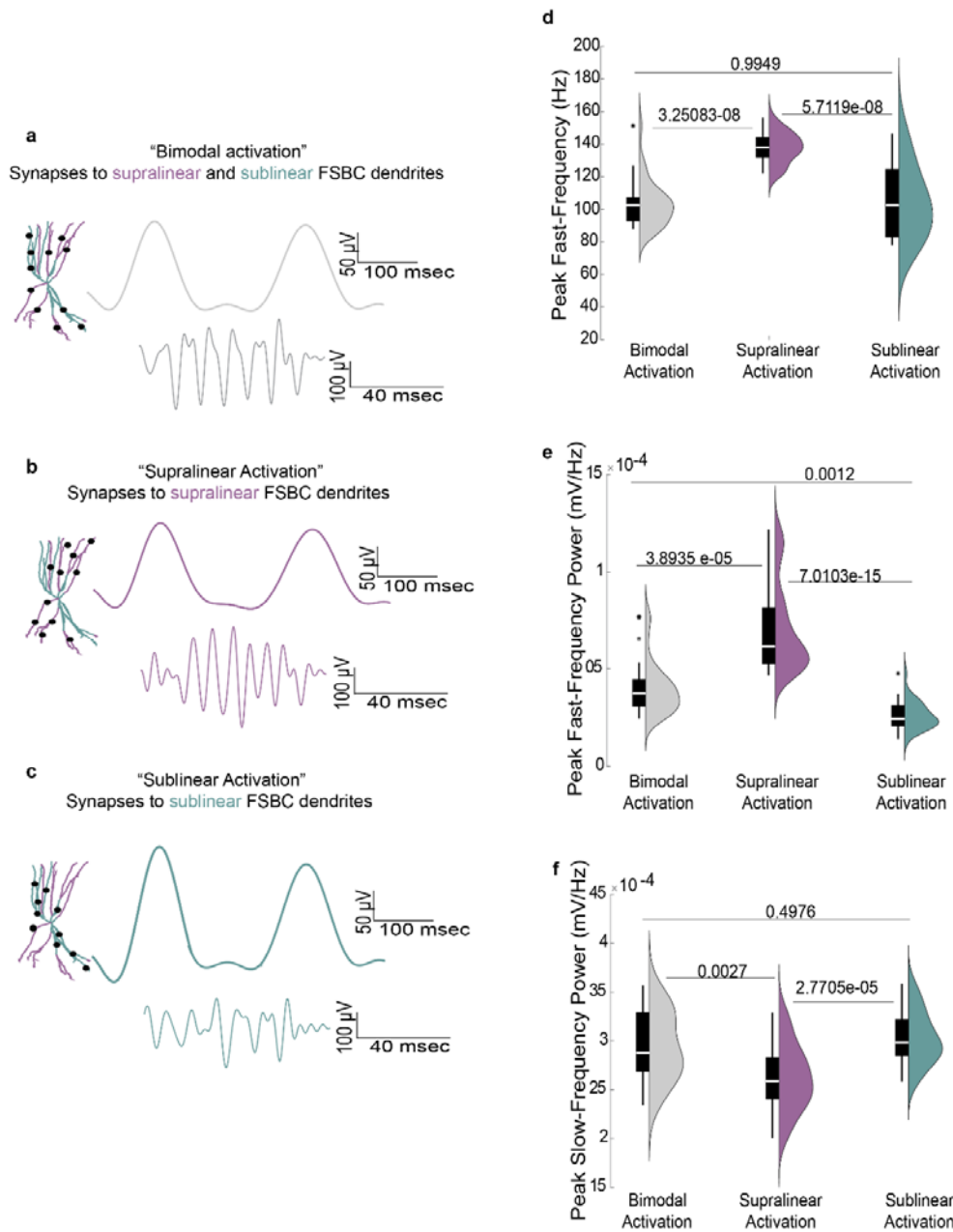
64 To test our hypothesis, we used a previously published biologically plausible hippocampal
65 microcircuit model²⁷ that includes compartmental biophysical models of pyramidal cells
66 (PCs) with reduced morphology²⁷ and FSBCs with anatomical reconstructions of bimodal
67 nonlinear dendritic trees, as in^{19,27} (**TablesS1-5, Fig.1a**). Upon activation with a theta-like
68 input as per^{28,29}, our microcircuit exhibited a slow oscillatory component coupled with a fast
69 one (**Fig.1a,d**). In our control experiment (bimodal activation), synapses to FSBCs were
70 placed in randomly chosen both supralinear and sublinear branches (**Fig.1a,d, 2a**). We
71 investigated how the network would respond when keeping the amount of synaptic contacts
72 constant but activating either only randomly chosen supralinear branches (**Fig.1e, 2b**) or
73 only sublinear branches (**Figs.1f, 2c**) of FSBCs trees. Our model predicts that activation of
74 the supralinear branches of the FSBCs trees supports the fast oscillatory component
75 (**Fig.1e,2b**). In sharp contrast, activation of only sublinear branches enhances the power of
76 the slow LFP band (**Figs 1f, 2c**). Specifically, supralinear activation results in a higher fast
77 frequency and fast peak-frequency power compared to both bimodal and sublinear activation
78 conditions (**Fig.2d, e**). In contrast, sublinear activation massively decreases the fast peak-
79 frequency power compared to both bimodal and supralinear activation (**Fig.2d**), as well as
80 the fast peak-frequency and slow power compared to supralinear activation (**Fig.2e,f**). To
81 assess the robustness of the differential impact of supralinear vs sublinear dendritic
82 activation in the LFP bands, we performed a sensitivity analysis on the synaptic parameters
83 and input features. In all cases supralinear activation enhanced the peak power and peak
84 frequency power of the fast LFP component whereas sublinear activation resulted in higher
85 slow power compared to supralinear activation (**Fig.S2**).

86

87 **Figure 1. Bimodal dendritic integration in FBCs modulate memory-related**
88 **hippocampal oscillations.** Schematic illustration of the hippocampal microcircuit model. A
89 population of 20 PCs and 2 FSBCs is activated by a theta (4 Hz) input for 1000 msec. An

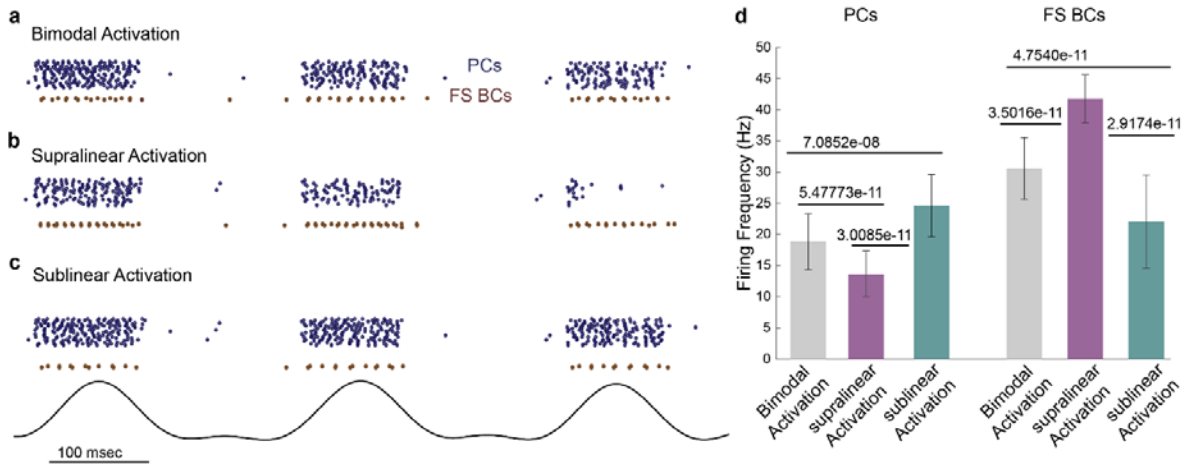


90 *LFP electrode is positioned nearby the PCs somata. Upon activation the model exhibits slow*
 91 *(bandpassed at 3-10 Hz) and fast (bandpassed at 30-200 Hz) LFP bands. The arrow*
 92 *indicated the in-silico electrode position. FSBCs are equipped with bimodal nonlinear trees*
 93 *as per Tzilivaki et al., 2019. b-c.* Representative input-output curves from supralinear (**b**) and
 94 sublinear (**c**) dendritic branches in FSBC models, in response to synaptic stimulation.
 95 Increasing numbers of synapses (from 1 to 20 with step $\Delta = 1$) are uniformly distributed in
 96 every stimulated branch and are activated with a single pulse. The y-axis shows the
 97 amplitude of the dendritic EPSP caused by synaptic activation while the x-axis shows the
 98 expected EPSP amplitude that would result from the linear summation of synaptic EPSPs.
 99 The dashed line indicates linear summation. Insets show representative traces. Panels were
 100 adopted from Tzilivaki et al., 2019. **d-f.** Power Spectrum Density (PSD) plots upon bimodal
 101 (**d**), supralinear (**e**) and sublinear (**f**) activation. The number of activated synapses remain
 102 identical for all conditions. Synapses were placed in randomly chosen supralinear and
 103 sublinear branches (**d**) or in either randomly chosen supralinear (**e**) or sublinear (**f**)
 104 branches. Activation of the supralinear dendrites (**e**) supports the fast LFP signature while
 105 sublinear activation (**f**) promotes slow LFP power. Data from 30 random simulation trials.



130 **Figure 2. LFP frequency and power are regulated by FSBC nonlinear dendritic**
 131 **activation.** (a-c) Schematic illustration of the activation protocols and representative traces
 132 of the evoked LFP bandpassed at slow (theta 3-10 Hz) and fast (30-200 Hz) frequencies.
 133 The same number of synapses targets either both types of nonlinear dendrites (bimodal
 134 activation) (a) or only supralinear (b) or only sublinear (c). (d-f) Comparison of the peak fast-
 135 frequency (d) and the peak powers of the fast (e) and slow (f) LFP components. Data from
 136 30 random simulation trials. Synaptic activation of supralinear dendrites of the FSBCs
 137 bimodal trees results in a higher peak fast-frequency and increased fast-frequency peak
 138 power, while reducing the peak power of slow oscillations compared to sublinear dendrite
 139 activation. Statistical comparisons across multiple groups were performed using the Kruskal-
 140 Wallis test followed by a post-hoc correction for multiple comparisons, suitable for data with
 141 unequal variance.

142 Given that the number of synapses remains consistent across all three activation scenarios
143 (bimodal, supralinear, and sublinear), we sought to understand the factors driving the
144 observed LFP modulation. To achieve this, we analyzed the spiking activity of both the PC
145 and FSBC populations under these conditions. Our analysis revealed that supralinear
146 activation led to higher spike rates in FSBCs, resulting in decreased firing of the PC
147 population compared to both bimodal and sublinear activation conditions. Conversely,
148 activation of sublinear branches in FSBCs reduced their firing rates, thereby disinhibiting the



149 PC population (Fig.3).

150

151 **Figure 3. Supralinear and Sublinear FSBC dendrites differentially modulate the E/I**
152 **balance in the microcircuit. (a-c).** Representative raster plots showing the spiking activity
153 of PCs (blue) and FSBCs (brown) across indicative theta cycles under different dendritic
154 activation conditions: bimodal (a), supralinear (b), or sublinear (c). (d) Activation of a fixed
155 number of synapses on randomly selected supralinear dendrites significantly increases the
156 firing frequency of FSBCs, leading to a reduction in the activity of PCs when compared to
157 bimodal (supralinear and sublinear) or purely sublinear activation. Conversely, activation of
158 randomly selected sublinear dendrites decreases the firing frequency of FSBCs, resulting in
159 disinhibition of the PCs. Data are based on 30 random simulation trials. Pairwise
160 comparisons were performed using the Mann–Whitney U test.

161

162 These observations demonstrate that FSBCs can adapt their firing patterns when activated
163 through either supralinear or sublinear branches, despite receiving an equivalent synaptic
164 input. Supralinear dendritic branches are characterized by larger volumes and lower input
165 resistance¹⁹ which facilitates enhanced forward propagation of signals. In contrast, activation
166 of sublinear branches, which have smaller volumes and therefore higher input resistance¹⁹,
167 restricts forward propagation (Fig.S1f-g), leading to decreased firing rates of FSBCs.
168 Consequently, this modulation alters the excitation to inhibition (E/I) balance within the
169 network, thereby influencing the characteristic oscillatory activity observed in the LFP.

170 We further explored how altering the dendritic integration profile of FSBCs, specifically by
171 manipulating them to possess purely supralinear or sublinear trees, impacts network
172 behavior compared to the control (bimodal) trees (Fig.S3a-b). Leveraging the distinct
173 morphological features of supralinear and sublinear branches in our bimodal FSBCs
174 reconstructions, we adjusted the dendritic morphologies as per¹⁹. When FSBCs were

175 equipped with purely supralinear dendritic trees, we observed enhanced fast frequency and
176 power compared to both bimodal and sublinear tree configurations. This configuration also
177 maximized the firing response of FSBCs (**Fig.S3a,c-h**). Conversely, FSBCs with purely
178 sublinear dendritic trees present reduced spike rate which increased the PCs activity
179 (**Fig.S3h**). Sublinear FSBC trees exhibited increased slow power and decreased fast power
180 and lower fast power compared to supralinear trees (**Fig.S3b-g**).

181 These simulations underscore that FSBCs take advantage of their bimodal nonlinear
182 dendritic trees by dynamically utilizing their supralinear and sublinear dendrites to regulate
183 the E/I balance within the network, thereby orchestrating distinct oscillatory behaviors under
184 equivalent synaptic input conditions. Importantly, activating either only supralinear or only
185 sublinear branches of a bimodal tree (**Figs.1-2**) exhibits similar phenotypic responses to
186 hypothetical configurations of purely supralinear or purely sublinear trees (**Fig.S3**). This
187 further supports the notion that the bimodal nonlinear nature of FSBCs dendrites allows for
188 flexible modulation of network activity and oscillatory patterns crucial for hippocampal
189 mnemonic functions.

190 Apart from the type of dendritic integration, the spatial arrangement of synapses also
191 influences the firing characteristics³⁰. It's well-established that supralinear dendrites tend to
192 enhance clustered synaptic allocation, whereas sublinear dendrites prefer dispersed
193 activation. For FSBCs, it has been observed that dispersed synaptic activation leads to
194 higher firing frequencies compared to clustered^{18,19,31}. This phenomenon is influenced by the
195 co-existence of sublinear along with supralinear branches, coupled with their small size and
196 the presence of A-type potassium channels^{19,22,31}, which discourages preference for
197 clustered inputs. To investigate how synaptic clustering affects the oscillatory behavior of our
198 network, we simulated the activation of the same number of synapses as in our disperse
199 protocols (as in **Fig.S3**) but now clustered in a few randomly chosen dendrites (**Fig.S4**). As
200 anticipated, clustered activation of sublinear FSBC trees significantly reduced their firing
201 rates while maximizing the E/I balance in the network. Conversely, clustering synapses in
202 supralinear trees enhanced FSBC firing rates compared to both bimodal and sublinear
203 clustering configurations, while also decreasing the firing rates of the PCs (**Fig.S4j**). At the
204 oscillatory level, akin to our simulations with dispersed synaptic activation, clustered
205 synapses in supralinear FSBC trees enhanced fast LFP components, whereas synaptic
206 clustering in sublinear trees boosted the slow LFP power (**Fig.S4a-i**). These findings
207 underscore the dual impact of dendritic morphology and synaptic spatial arrangement on
208 neuronal firing patterns and network oscillatory dynamics. They highlight the intricate
209 mechanisms by which FBCs can dynamically modulate their responses and contribute to the
210 regulation of network excitability and oscillatory activity crucial for hippocampal function.

211 Finally, we analyzed the Phase-Amplitude Coupling (PAC),³² to check the slow-fast
212 oscillation coupling in the LFP across all cases (**Fig.S5**). Indeed, the LFP response aligns
213 with experimental findings, indicating that slow activity entrains hippocampal networks to
214 slow-fast coupling (**Fig.S5a**)^{5,9,28,33-36}. Activation of either supralinear or sublinear branches
215 did not alter the coupling between the two oscillatory components (**Fig.S5b-f**). However,
216 coupling was enhanced when synapses were clustered on fully sublinear dendritic trees of
217 FSBCs. Conversely, coupling was reduced when similar clustering occurred on supralinear
218 FSBC dendritic trees (**Fig.S5g-j**). These results indicate that as the power and frequency of
219 the fast component decrease, it becomes more synchronized with the slower component.

220 Overall, while the role of interneurons in hippocampal memory-related oscillations is
221 established^{13,16,18,26}, there remains a significant gap in understanding the cellular and
222 subcellular mechanisms that enable these neurons to flexibly control memory-related
223 rhythms. Recent studies suggest the involvement of PV+ interneuron dendrites in fast

224 oscillations^{20,37,38}, yet a direct link between interneuronal dendritic integration and their
225 impact on slow and fast hippocampal memory-related rhythms is lacking. Our biophysical
226 modeling provides novel insights showing that hippocampal FSBCs, a prominent subtype of
227 PV+-positive interneurons, exhibit distinct firing patterns that modulate the excitatory-
228 inhibitory (E/I) balance in networks independent of synaptic input quantity. Specifically,
229 activation of supralinear dendritic branches in bimodal FSBCs (**Fig.1,2,S1**) reduces the E/I
230 balance (**Fig.3**), thereby promoting fast oscillatory activity associated with memory
231 consolidation (**Fig.1,2**). In contrast, activation of sublinear dendritic branches increases the
232 E/I balance (**Fig.3**), enhancing the slow LFP signature (**Figs.1,2**), linked to memory
233 encoding. To fully explore the impact of interneuron dendrites on memory-related
234 oscillations, it is crucial to investigate the diversity among hippocampal interneurons^{12,13,15,26}.
235 Beyond FSBCs, other subclasses of PV+ interneurons and different inhibitory classes (e.g.
236 SOM+ and VIP+ interneurons) are active during distinct memory-related rhythms^{12,13}, yet
237 their specific dendritic integration profiles remain poorly characterized. Future studies should
238 thus aim to dissect how dendritic nonlinear integration across different interneuron
239 types^{12,13,15,16} and PCs³⁹ modulate memory-related oscillations. Future experimental efforts
240 should aim to elucidate whether distinct hippocampal and cortical inputs selectively target
241 the supralinear or sublinear branches of bimodal FSBCs trees. Although connectivity
242 patterns between hippocampal (e.g. CA3) and extrahippocampal (e.g. entorhinal
243 cortices) populations to FSBCs are documented during fast oscillations^{12,13,31,40}, it remains
244 unclear whether neurons from the same or different regions preferentially target these two
245 types of nonlinear dendrites. Investigating the potential differential targeting of FSBCs'
246 supralinear and sublinear branches during distinct memory stages, such as encoding versus
247 consolidation, could significantly enhance our understanding of how FSBCs dynamically
248 regulate memory-related rhythms by leveraging their diverse dendritic architectures across
249 different oscillatory activity patterns. Our simulations suggest that bimodal nonlinear dendritic
250 processing in FSBCs could be critical to drive different memory stages and, therefore,
251 influence behavioral states.

252

253 **Author contributions:** AT and DS conceived the study. AT designed and run the
254 simulations, analyzed the data, prepared the figures and wrote the manuscript. MEL and DS
255 provided senior conceptual input on the study and methodology. DS funded and supervised
256 the project. All authors wrote/edited the final version of the manuscript.

257 **Acknowledgements:** A.T. was supported by the DFG with the SFB1315-2 TP A01 Brenda
258 Milner Award and the Einstein Center for Neurosciences Berlin Fellowship. M.E.L. was
259 supported by the European Research Council (101055340, ERC AdG, Cortical Coupling).
260 D.S. was supported by the Einstein Foundation Berlin, the European Research Council
261 (ERC) under the Europeans Union's Horizon 2020 research and innovation program
262 (BrainPlay grant, agreement no. 810580), the German Research Foundation (Deutsche
263 Forschungsgemeinschaft [DFG], SFB-958 – project 184695641, project 431572356, FOR
264 3004 – project 415914819, SFB 1315 – project 327654276 and under Germany's Excellence
265 Strategy – Exc-2049-390688087 NeuroCure), and the Federal Ministry of Education and
266 Research (BMBF, SmartAge – project 01GQ1420B). We thank Michalis Pagkalos, Jeremie
267 Sibille, Nikolaus Maier, and John Tukker for helpful discussions, comments and
268 proofreading, Nelson Rebola, Yann Zerlaut, Yiota Poirazi, for comments on an earlier version
269 of the manuscript and Daniel Parthier for feedback on the statistical analyses.

270

271 **Code and Data availability**

272 Scripts and datasets required to reproduce the results and figures, as well as all statistical
273 analyses, are publicly accessible in www.github.com/AlexandraTzilivaki/Tzilivakietal2024

274 **Competing interests**

275 The authors declare no competing interests.

276

277

Methods

278 **Model implementation and availability**

279 Simulations were conducted using NEURON (v7.6)⁴¹ on a High-Performance Computing
280 Cluster, utilizing 111 CPU cores on a 64-bit CentOS Linux operating system. All
281 codes/scripts and datasets required to reproduce the results and figures, as well as all
282 statistical analyses, are publicly accessible in
283 www.github.com/AlexandraTzilivaki/Tzilivakietal2024

284

285

286 **Neuronal populations**

287 1. Fast Spiking Basket Cells (FSBCs)

288 Two multi-compartmental biophysical models of CA3 FSBCs were employed, adopted
289 from Tzilivaki et al. (2019)¹⁹. These FSBCs models include detailed anatomical
290 reconstructions of somata and dendritic trees taken from Neuromorpho database
291 (originally published in Tukker et al. 2007⁴²), (**Figure S1**). Both FSBCs feature bimodal
292 nonlinear dendritic branches, characterized by both supralinear and sublinear branches.
293 They are equipped with fast voltage-dependent sodium channels (gna_{fin}), delayed
294 rectifier potassium channels (gk_{d_{in}}), slow inactivation potassium channels (gslow_{in}),
295 slow calcium-dependent potassium channels (gk_{ca_{in}}), A-type potassium channels in
296 proximal and distal dendritic regions (gk_{ad_{in}}, gk_{ap_{in}}), h-currents (gh_{in}), and L-, N-, and
297 T-type voltage-activated calcium channels (gca_l, gca_n, and gca_t, respectively). These
298 models have been extensively validated against experimental data and accurately
299 capture the intrinsic features and electrophysiological responses of hippocampal FSBCs
300 (See original reference¹⁹ and Supplementary Information). The mean dendritic diameter
301 and total dendritic length were measured for the supralinear and sublinear dendrites of
302 the two FSBCs morphological reconstructions. Dendritic volume was calculated as per
303 Tzilivaki et al. (2019)¹⁹ using the following formula:

$$V = \pi * \left(\frac{\text{diameter}}{2}\right)^2 * \text{length} (\mu\text{m}^3)$$

304 To causally manipulate the dendritic morphologies of FSBCs to generate fully supralinear or
305 sublinear trees (Figure S2), we performed causal manipulations according to the approach
306 described in Tzilivaki et al. (2019)¹⁹. We fixed the diameter and length of all dendrites to
307 create trees with average supralinear or sublinear dendritic volume (**Figure S1B**), which
308 dictated the integration mode as shown in the original modeling publication. Dendritic Input
309 Resistance was calculated using the following formula:

310

$$R_{in} = \frac{DV}{I} \left(\frac{mV}{nA} \right)$$

311 where $I = -100$ pA injected in each dendritic branch and DV is the generated
312 IPSP.

313

314 For more detailed information about the FSBC models, please refer to the relevant
315 publication¹⁹ and **Tables S1-2, 4-5**.

316

317 2. Pyramidal Cells (PCs)

318 Biophysically relevant hippocampal PC models (n = 20) were adopted from Hadler et al.
319 (2024)²⁷. These models consist of somata and proximal, distal, and basal dendritic branches.
320 PCs include a Ca²⁺ pump and buffering mechanism, Ca²⁺ activated slow AHP and medium
321 AHP potassium (K⁺) currents, an HVA L-type calcium (Ca²⁺) current, an HVA R-type
322 Ca²⁺ current, an LVA T-type Ca²⁺ current, an h-current, a fast sodium (Na⁺) current, a
323 delayed rectifier K⁺ current, a slowly inactivating K⁺ M-type current, and a fast inactivating
324 K⁺ A-type current. These current mechanisms were non-uniformly distributed along the
325 somatodendritic compartments. They were validated based on *in vitro* data to replicate the
326 electrophysiological profile and basic dendritic architecture of hippocampal CA3 PCs^{27,43}.
327 The PC models do not include detailed nonlinear dendritic trees, as this was beyond the
328 scope of this study. Incorporating realistic anatomical reconstructions for PCs would have
329 significantly increased computational complexity and reduced simulation speed. For more
330 information, see Hadler et al. (2024)²⁷ and **Tables S3-5**.

331 **Synaptic properties**

332 The PC models were equipped with AMPA, NMDA, and γ -aminobutyric acid type A (GABAA)
333 synapses, while the FSBCs included Ca²⁺ permeable AMPA (CP-AMPA), NMDA, GABAA,
334 and autaptic GABAA synapses. The synaptic conductance values for every connection type
335 were calibrated based on experimental⁴⁴⁻⁴⁷ and modelling studies¹⁹ and are listed in **Table**
336 **S5**

337 To ensure the robustness of our finding we repeated the simulations upon increased or
338 decreased synaptic conductance values (15% change) (see sensitivity analysis Figure S2)

339 **Hippocampal Microcircuit**

340 The hippocampal microcircuit configuration was adopted from Hadler et al. (2024)²⁷. The
341 model consists of 20 PCs and 2 FSBCs. In each random simulation trial (n = 30), each PC
342 contacted up to seven (7) randomly chosen PCs with one AMPA and one NMDA synapse
343 activation per contact. Each FSBC received synaptic input from fifteen (15) randomly chosen
344 PCs in each simulation trial. Additionally, each PC received thirteen (13) feedback inhibitory
345 GABAergic inputs from each FSBC per simulation trial. Each FSBC formed five (5)
346 GABAergic synapses per simulation trial and was self-inhibited through autapses. For further
347 details, see the Simulation Paradigms chapter and Hadler et al. (2024)²⁷.

348 **Simulation Paradigms**

349 Input

350 The microcircuit is activated by a theta entrained presynaptic population as per Turi
351 et al., 2018⁴⁸. The input was modeled as an artificial presynaptic population (N=22)
352 using NEURON's VecStim function. The spike times of the presynaptic population
353 were generated using a sinusoidal theta like filter that was applied so to account for
354 theta like modulated spike times.

355 Thata like probability formula (as per⁴⁸):

$$p(t) = (\sin\left(2.0 * \pi * \frac{f_{\theta} * \text{spike}}{1000.0} + \text{phi}_{\theta}\right) + 1.0) / 2.0$$

356 Where:

- 357 • spike = the spike time in msec (float)
- 358 • f_theta = theta-cycle frequency in Hz. (float)

359 For the simulations shown in Figures 1-3 and Supplementary Figures 3-5, f_theta=4
360 Hz. For the sensitivity analysis simulations as shown in Supplementary Figure 2, we
361 changed the input the theta frequency to f_theta=5Hz.

- 362 • phi_theta= theta cycle phase in radians.

363 For the simulations shown in Figures 1-3 and Supplementary Figures 3-5,
364 phi_theta=0 (equal to 0 radians). For the sensitivity analysis simulations as shown in
365 Supplementary Figure 2, we shifted the input phase so phi_theta=0.5 (equal to 180
366 radians).

367

368 If the probability p(t) is greater than 0.7 a spike is generated for the specific artificial
369 neuron (n=22). Every input neuron has its own theta modulated spike train.

370

371 Each PC received input from 5 artificial presynaptic neurons, while each FSBC
372 received input from 7 artificial presynaptic neurons. Although the input was sufficient
373 to activate the PC population due to its reduced morphology, 7 artificial presynaptic
374 neurons were insufficient to evoke spiking activity in the FSBC models, given their
375 realistic complex anatomical reconstructions. This subthreshold activation was
376 selected to ensure that FSBCs were primarily engaged in the network due to the
377 local inputs they received from PCs.

378

379 1. Simulations

380 The microcircuit model was simulated for approximately 12,000 milliseconds (ms)
381 with a time step of 0.1 ms. The first 200 ms were excluded from the analysis to allow
382 the model to reach an equilibrium state. For the dispersed protocols, synapses to
383 FSBCs (both input and local PC-to-FSBC synapses) were randomly assigned to
384 dendrites, meaning one randomly chosen dendrite received one pair of NMDA and
385 CP-AMPA synapses. For the clustered protocol (Supplementary Figure S4), the
386 same total amount of synapses was placed in 4 randomly chosen dendrites (cluster
387 size: 5-7 synapses (per dendrite) Data represent the results (mean and standard
388 deviation values (std)) of thirty (30) random simulation trials for each protocol. In
389 every trial, the total number of synaptic contacts and the connectivity ratios remained
390 identical, but different randomly chosen neurons (from both PC and FSBC
391 populations) were connected to different random neurons. Additionally, in each trial,
392 different dendrites from both PCs and FSBCs were randomly chosen and synapses
393 were activated at different parts of the chosen dendrites. This approach ensured that
394 the results reflected the diversity, especially of the FSBCs trees, in bimodal activation
395 protocols. Furthermore, two different anatomical reconstructions were used for our
396 FSBC models to account for FSBCs morphological variability (see relevant chapter).

397

398 2. LFP simulation and Spectral analysis

399 To record the Local Field Potential (LFP), an *in silico* electrode was simulated based on
400 NEURON's extracellular function, following the modelling approach of Vladimirov et al.
401 (2013)⁴⁹. The electrode was placed close to the PCs somata and remained in the exact
402 same position throughout the execution of all protocols and simulation trials. The

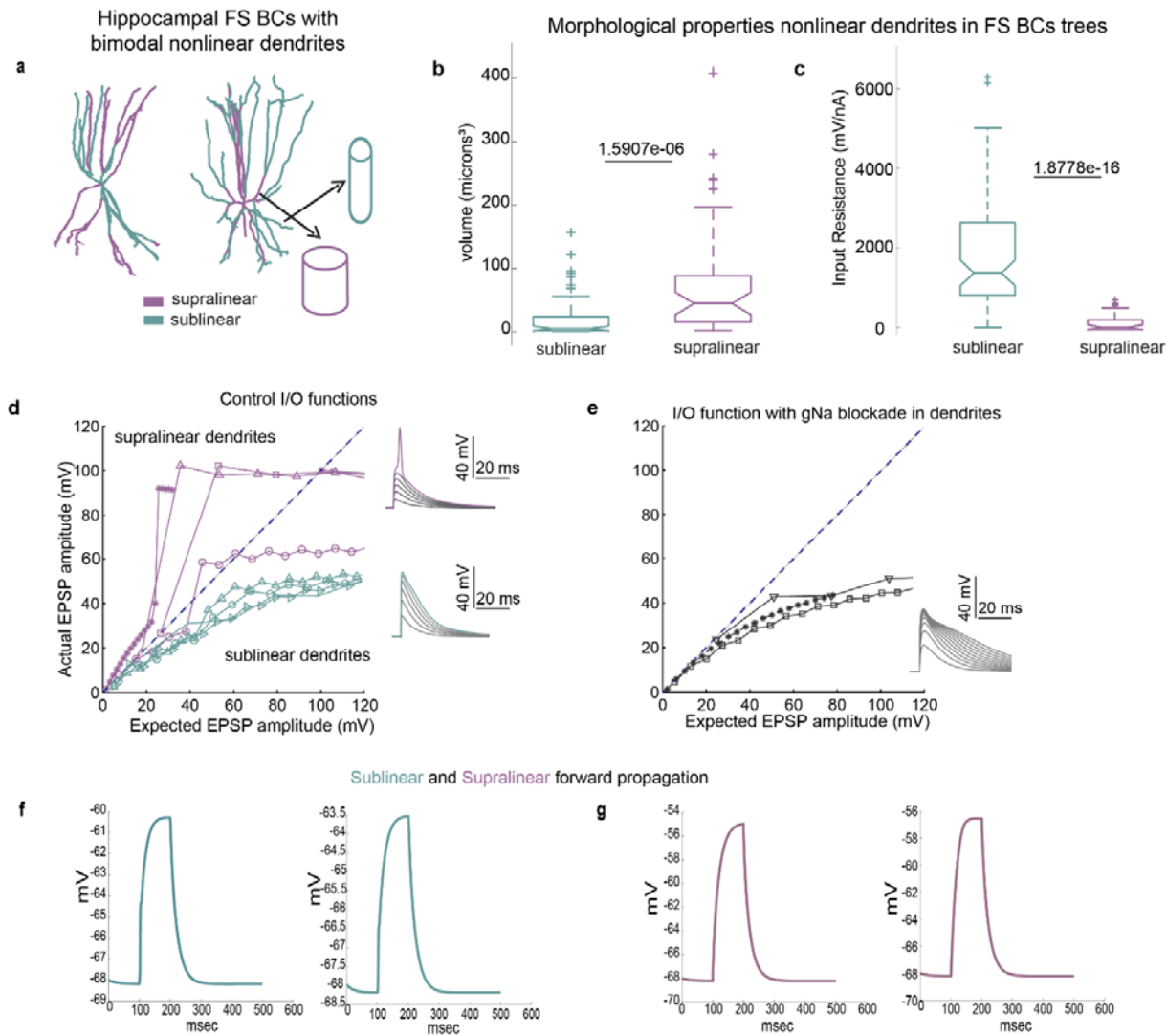
403 sampling frequency was set at 10 kHz. Despite the microcircuit model's small size, it
404 efficiently generated fast and slow oscillations comparable to experimental
405 observations^{5,11,32,35} while maintaining low computational complexity and demands.

406 The *in silico* LFP datasets were band-passed at two respective bands: slow (3 – 10 Hz)
407 and fast (30-200 Hz). Slow and fast Peak-Frequency powers and peak Fast frequency
408 were determined using custom-made MATLAB scripts (MATLAB, The MathWorks Inc.,
409 Natick, MA; Torrence and Compo 1998) utilizing the p-welch function (0.4 Hz resolution)
410 and visualized as Power-Frequency plots. Phase-Amplitude Coupling (PAC) analysis
411 was conducted using Comodulogram generation and the calculation of the modulation
412 index (MI) metric that were adopted from Tort et al. (2008)⁵⁰. Wavelet phase was
413 calculated at 15 levels from 1-15 Hz, and the amplitude at 50 levels from 30-180 Hz. The
414 MI was obtained by measuring the divergence of the observed amplitude distribution
415 from the uniform distribution.

416 **Statistical Analysis**

417 Statistical analyses for multigroup comparisons were performed using the Kruskal-Wallis
418 test, followed by a post-hoc correction for multiple comparisons (multcompare function
419 Matlab). For pairwise comparisons where data exhibited unequal variance, p-values
420 were calculated using the Mann-Whitney U test.

421 **Supplementary Information**

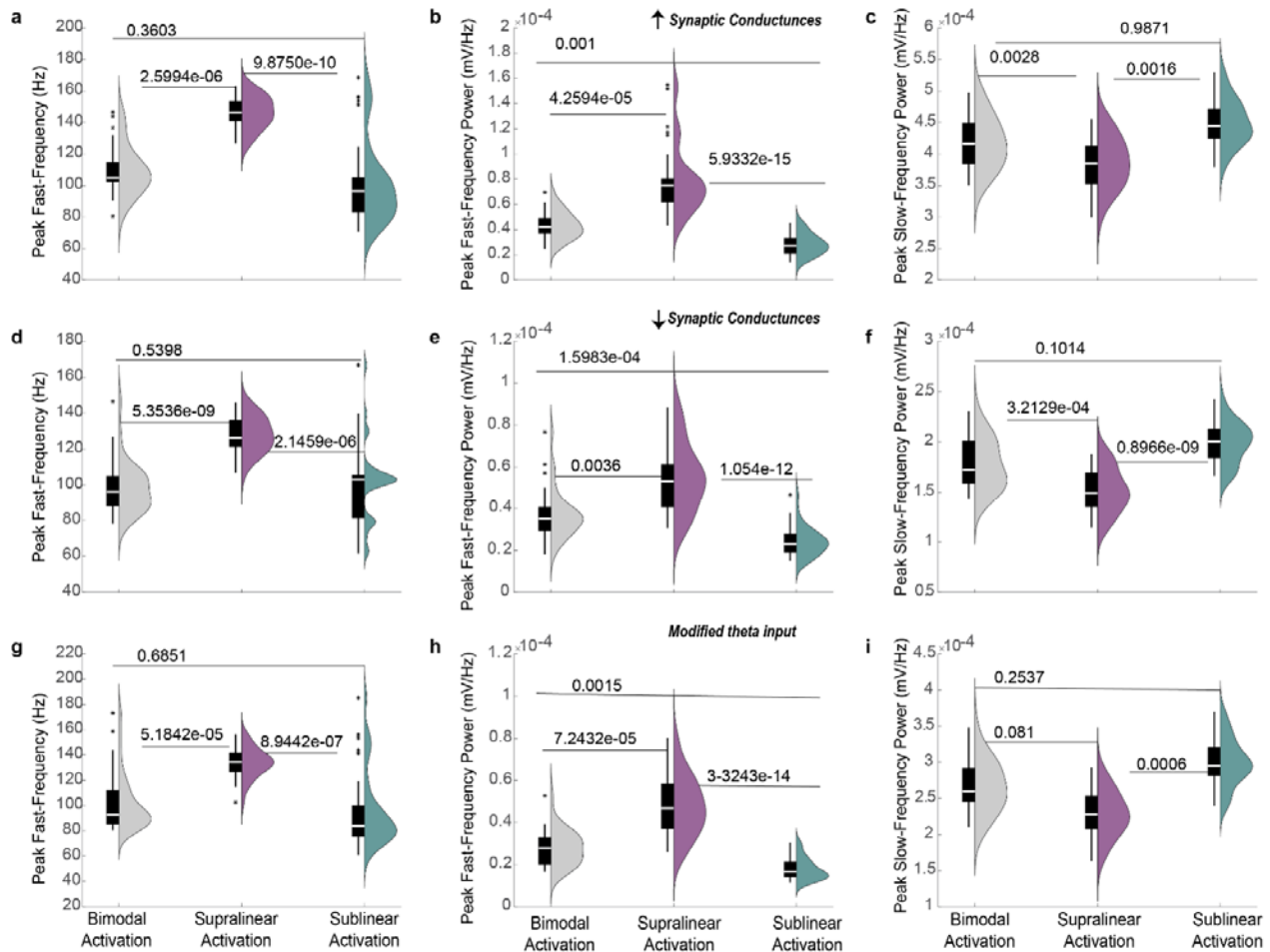


422 **Figure S1. Mechanisms of bimodal nonlinear dendritic integration in**
 423 **Multicompartmental Models of Hippocampal FSBCs.**

424 **a.** Illustration of the morphological characteristics of supralinear and sublinear dendrites in
 425 bimodal FSBC models. Supralinear dendrites (purple) are larger, whereas sublinear
 426 dendrites (blue) are longer and thinner. **b-c.** Discriminative features between dendrite types:
 427 supralinear dendrites have larger volumes (b) and lower input resistance (c) compared to
 428 sublinear dendrites. Statistical significance was determined using the Mann–Whitney U test.
 429 **d-e.** Supralinear dendrites (purple) are capable of generating local sodium-dependent
 430 spikes, whereas sublinear dendrites (blue) cannot (d). Blocking active sodium conductances
 431 in FSBC dendrites completely abolishes the supralinear mode (e). **f-g.** Forward propagation
 432 efficiency in bimodal nonlinear dendrites of FSBCs: Current injection (100 pA) at randomly
 433 selected dendrites and recording at the soma show that sublinear branches (f) propagate
 434 signals less effectively compared to supralinear branches (g). Panels a,d,e were adopted
 435 from ¹⁹

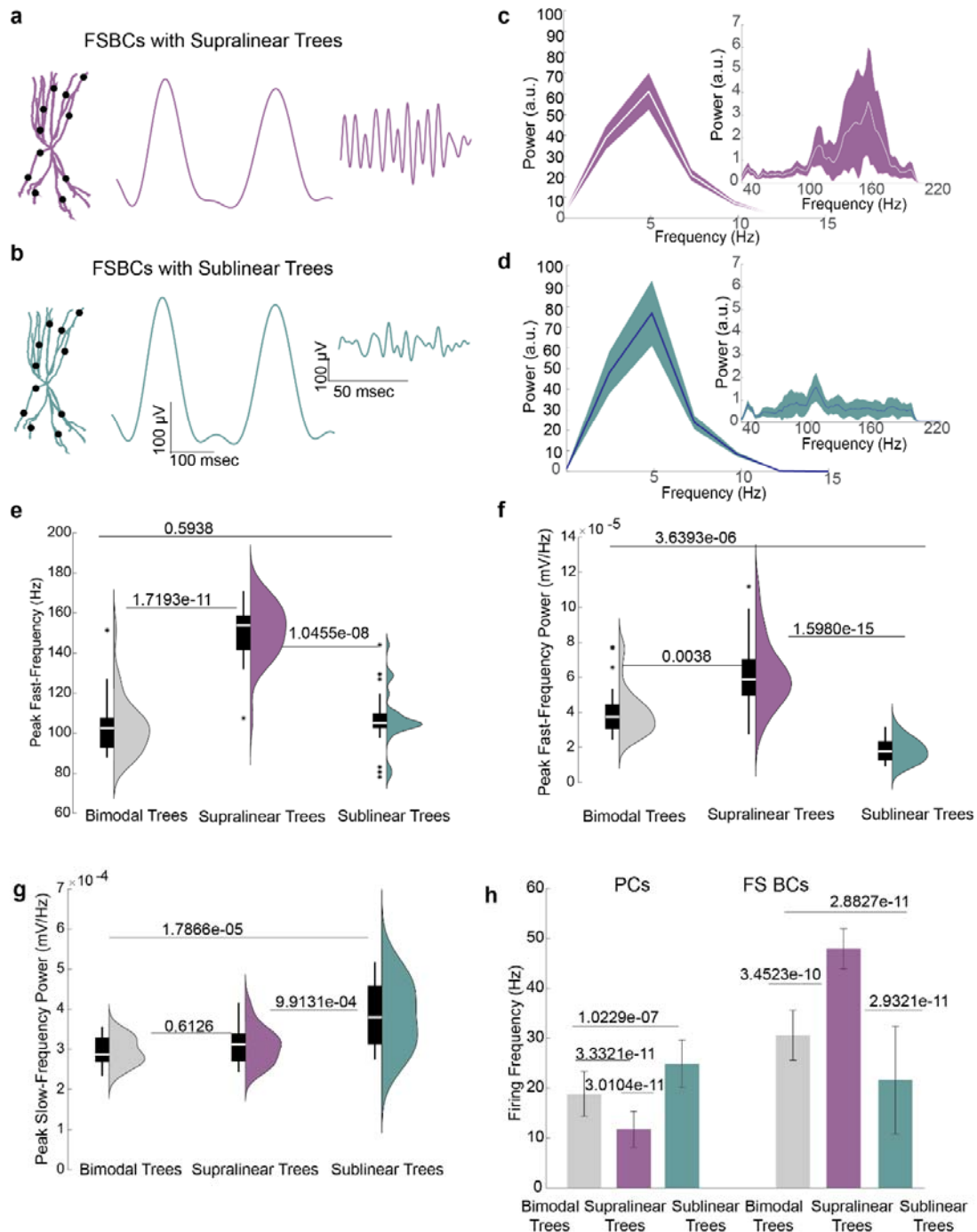
436

437



438 **Figure S2. Sensitivity Analysis on Synaptic and Input Parameters (Related to Figure**
 439 **2).** a-c. 15% increase in the synaptic conductance values (applied to both input and network
 440 synapses for/from both PCs and FSBCs) do not alter the enhancement of fast peak
 441 frequency and power observed with supralinear activation. d-f. 15% reduction of the synaptic
 442 conductance values (for both input and network synapses involving PCs and FSBCs) also
 443 maintain the observed increase in fast peak frequency and power upon supralinear
 444 activation. g-i. Modifications to input parameters (input phase shifted 180°, peak frequency 5
 445 Hz) similarly do not affect the enhancement of fast peak frequency and power driven by
 446 supralinear activation. Statistical analyses for multigroup comparisons were performed using
 447 the Kruskal-Wallis test, followed by a post-hoc correction for multiple comparisons.

448

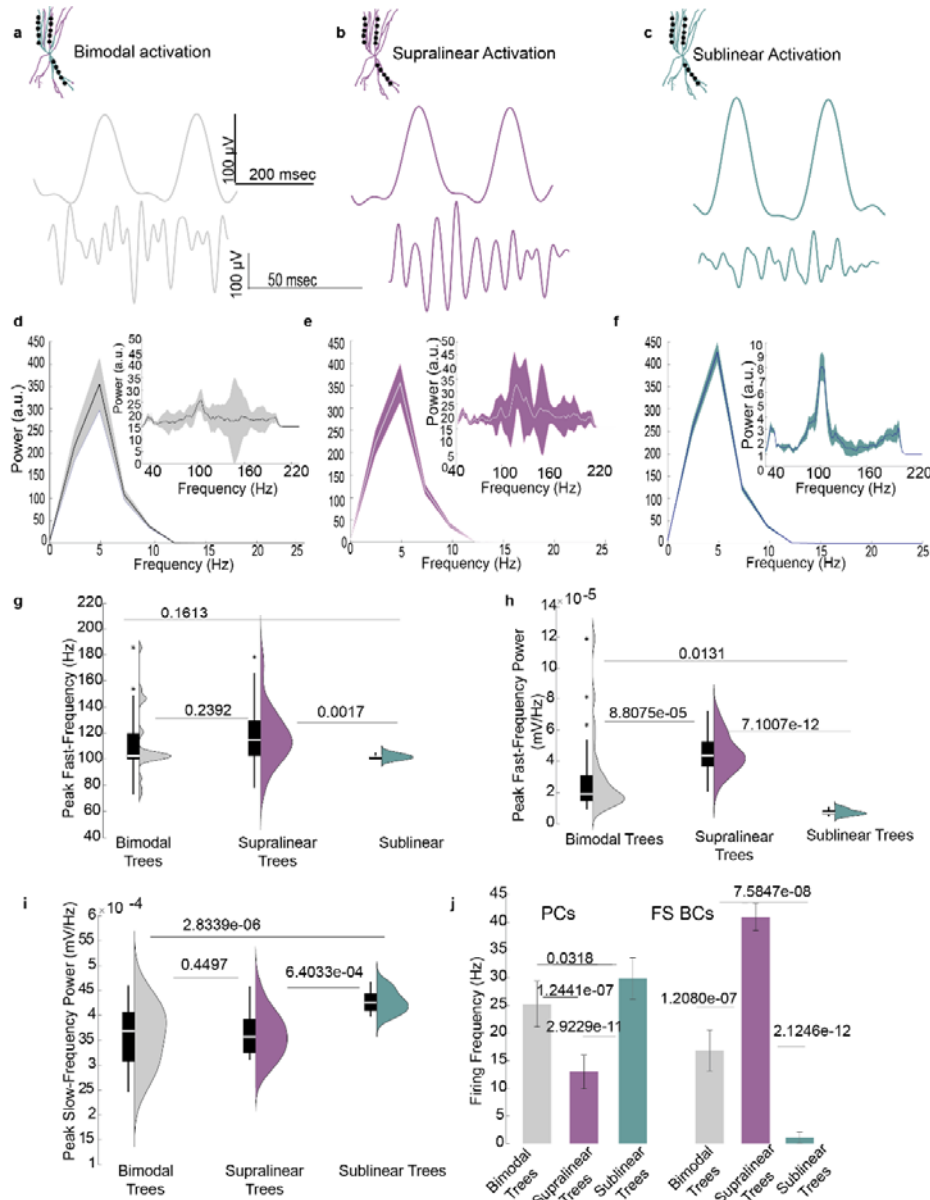


449 **Figure S3. Differential Modulation of Slow and Fast LFP Components by Supralinear**
 450 **and Sublinear FSBC Dendritic Trees.**

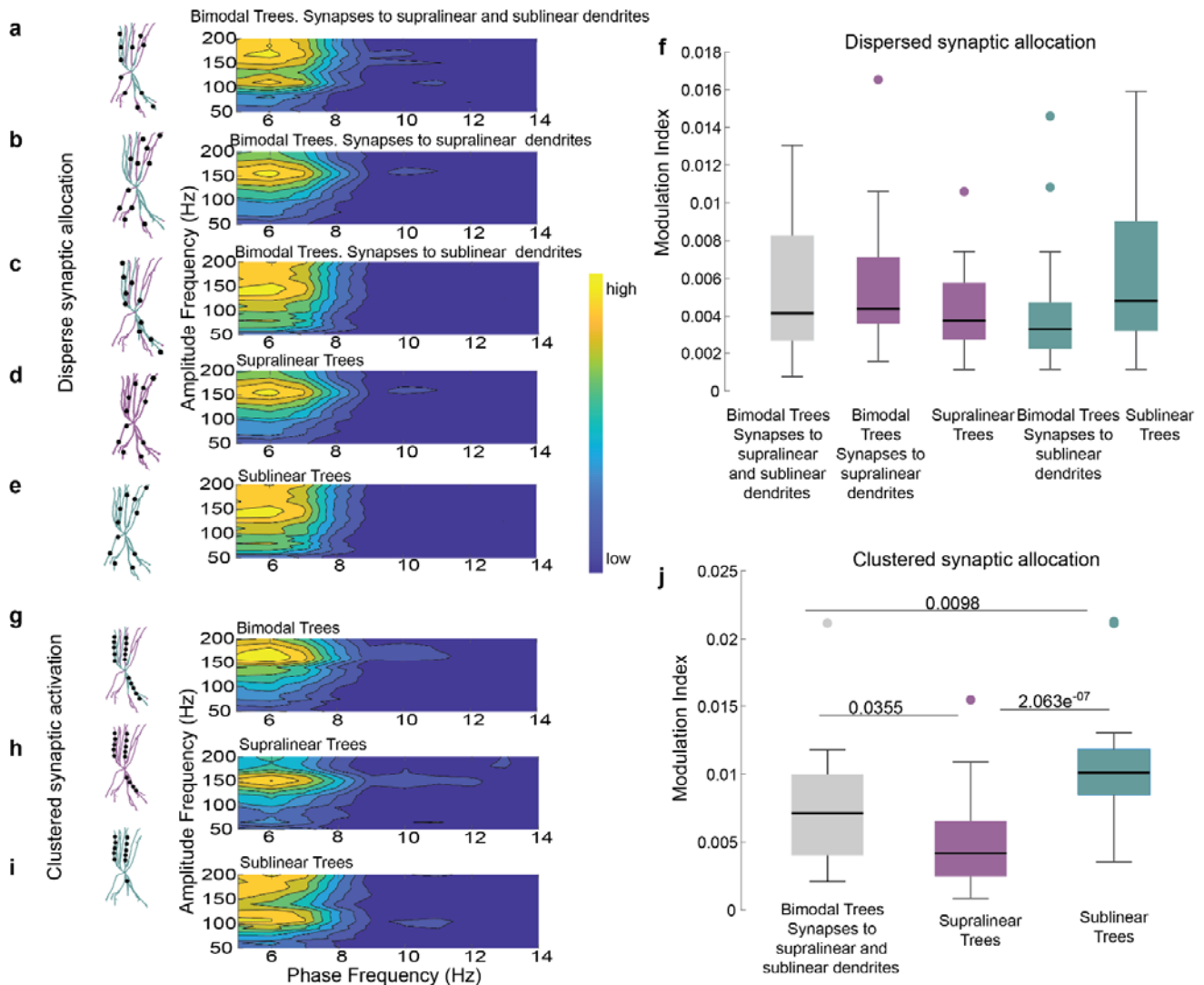
451 **a.** Activation of FSBCs equipped with purely supralinear dendritic trees, showcasing
 452 representative LFP traces bandpassed at slow (3-10 Hz) and high (30-200 Hz) frequencies.
 453 **b.** Similar to **a** but displaying activation of FSBCs with purely sublinear dendritic trees. **c-d.**
 454 Power Spectrum Density (PSD) plots of the LFP evoked when FSBCs are equipped with

455 purely supralinear (c) or purely sublinear (d) dendritic trees, highlighting differences in
 456 frequency response. **e-g.** Comparative analysis of the peak fast-frequency (e) and peak
 457 power of fast (f) and slow (g) oscillations for FSBCs with bimodal (grey), supralinear (purple),
 458 or sublinear (blue) dendritic trees. Data are derived from 30 random simulation trials. **h.**
 459 Firing activity of the PCs and FSBCs populations within the microcircuit network across 30
 460 random simulation trials. Activation of supralinear FSBC dendritic trees results in a
 461 decreased E/I balance compared to both bimodal (control) and sublinear trees. Statistical
 462 analyses for multigroup comparisons were conducted using the Kruskal-Wallis test followed
 463 by a post-hoc correction for multiple comparisons. Paired comparisons and p-values were
 464 calculated using the Mann-Whitney U test for data with unequal variance.

465



466 **Figure S4. Impact of Clustered Synaptic Activation on LFP and E/I Balance in Bimodal,**
 467 **Supralinear, and Sublinear FSBC Dendritic Configurations.** **a.** Activation of FSBCs with
 468 bimodal nonlinear dendrites (control configuration), showing representative LFP traces for
 469 slow (3-10 Hz) and fast (30-200 Hz) frequencies. Synapses are clustered in a few randomly
 470 chosen supralinear or sublinear branches. **b.** Activation of FSBCs with purely supralinear
 471 dendritic trees, showing LFP traces under clustered synaptic activation. **c.** Activation of
 472 FSBCs with purely sublinear dendritic trees, similar to conditions in **a** and **b**, illustrating the
 473 effect of clustered synaptic activation on LFP traces. **d-f.** Power Spectrum Density (PSD)
 474 plots for LFPs under clustered synaptic conditions in FSBCs with bimodal (**d**), supralinear
 475 (**e**), and sublinear (**f**) dendritic configurations. **g-i.** Comparison of peak frequency (**g**) and
 476 peak power for the fast LFP component (30-200 Hz) (**h**), and peak power for the slow LFP
 477 component (i), across dendritic configurations. **j.** Firing activity of PC and FSBC populations
 478 in the microcircuit network from 30 random simulation trials. Clustering in supralinear FSBC
 479 dendritic trees decreases the E/I balance in the network compared to bimodal (control) or
 480 sublinear trees. Statistical analyses for multigroup comparisons were conducted using the
 481 Kruskal-Wallis test followed by a post-hoc correction for multiple comparisons. Paired
 482 comparisons and p-values were calculated using the Mann-Whitney U test for data with



483 unequal variance.

484

485 **Figure S5. Slow-Fast Oscillation Coupling in the Microcircuit Model Under Various**
 486 **Dendritic and Synaptic Configurations in FSBCs. a-e.** Representative comodulograms
 487 illustrating the slow-fast coupling for the protocols detailed in Figures 2 and S3. These
 488 visualizations provide insights into the phase-amplitude coupling dynamics under different
 489 synaptic and dendritic configurations. Data from 30 random simulation trials are represented.
 490 **f.** Coupling analysis shows that synaptic distribution in a dispersed configuration across
 491 bimodal, purely supralinear, or purely sublinear FSBC dendritic trees does not affect slow-
 492 fast oscillation coupling. **g-i.** Similar to a-e but showcasing comodulograms for a clustered
 493 synaptic arrangement (detailed in Figure S4), using the same number of synapses as in the
 494 dispersed experiments. **j.** MI indicates that slow-fast oscillation coupling decreases when
 495 synapses are clustered in purely sublinear dendritic trees compared to other configurations.
 496 Multigroup comparisons were performed using the Kruskal-Wallis test followed by a post-hoc
 497 correction for multiple comparisons for multi-group data with unequal variance. This
 498 statistical approach was chosen to accommodate the diversity in the data from 30 random
 499 simulation trials.

500

Table S1. Active properties of Fast Spiking Basket Cell (FSBC) Models 501 *val
ues

Ion channel (S/cm ²)	Soma	Axon	Proximal dendrites	Distal Dendrites
Na _v	0.396	1.296	0.018	0.014
H _v	0.00001	X	x	X

Table S2. Passive properties of FSBCs

	Soma	Axon	Proximal dendrites	Distal Dendrites
Leak conductance (g _{pas}) ⁵³	1.315e-4 X S/cm ² X	3.55e-6 S/cm ²	x x	1.315e-4 X S/cm ² X
Resting Membrane Potential (e _{pas}) ^{53,54}	-68 mV	-68 mV	-68 mV	-68 mV
Membrane capacitance (cm) ⁵³	1.2 uf/cm ⁻² X	1.2 uf/cm ⁻²	1.2 uf/cm ⁻² x	1.2 uf/cm ⁻² 0.00216
Axial Resistance (Ra) ⁵³	172 ohm/ cm	172 ohm/ cm	142 ohm/ cm	142 ohm/ cm
Can _v	x	X	0.00003	0.00003
Cat _v	x	X	0.0002	0.0002
Calcium buffering dynamics	Yes	No	Yes	Yes

513

514

Table S3. Passive Parameters and Active Conductance Values of the Pyramidal Cell (PC) Model

Mechanism	Soma	Proximal Apical	Distal Apical	Basal
-----------	------	-----------------	---------------	-------

	Dendrite(n=1)	Dendrites (n=2)	Dendrites (n=2)
Leak conductance [S/cm ²]	0,0002	0,0002	0,0002
Na ⁺ conductance [S/cm ²]	0,0105	0,0084	0,0084
Delayed rectifier K ⁺ conductance [S/cm ²]	0,00086	0,00086	0,00086
Proximal A-type K ⁺ conductance [S/cm ²]	0,0075	0,015	-
Distal A-type K ⁺ conductance [S/cm ²]	-	-	0,04875
M-type K ⁺ conductance [S/cm ²]	0.06	0.06	-
I _h conductance [S/cm ²]	0.00005	0.0001	-
L-type Ca ²⁺ conductance [S/cm ²]	0.0007	0.00003	-
R-type Ca ²⁺ conductance [S/cm ²]	0.0003	0.00003	-
T-type Ca ²⁺ conductance [S/cm ²]	0.00005	0.0001	-
Ca ²⁺ -dependent sAHP K ⁺ conductance [S/cm ²]	0.0015	0.001	-
Ca ²⁺ -dependent mAHP K ⁺ conductance [S/cm ²]	0,9	0,03	-
Membrane capacitance C _m [μF/cm ²]	1	1	1
Membrane resistance R _m [Ohm cm ²]	6000	6000	6000
Axial resistance R _a [Ohm cm]	150	150	150

515 * values as per ²⁷

516

Table S4. Electrophysiological properties of the PCs and FSBCs models

	Value
Rheobase (pA)	200 (PC) / 150 +/- 10 (FSBC)
Input Resistance (MΩ)	142 (PC) / 97 +/- 30 (FSBC)
Spike Threshold (mV)	-43,11 (PC) / -37 +/- 1 (FSBC)
Spike Overshoot (mV)	30 (PC) / 48 +/- 1 (FSBC)
Resting Membrane Potential (mV)	-70 (PC) / -68 (FSBC)

517

Table S5. Synaptic conductance weight values of the PC and FSBC models.

Synapse Type	Pyramidal model	FSBC model
INPUT AMPA	0,00272	-
INPUT NMDA	0,0053	0.00032
INPUT CA ⁺⁺ PERMEABLE (CP)-AMPA	-	0.00075
AMPA	0,0017	-
CP-AMPA	-	0,0034

NMDA	0,0051	0.00144
GABA	0,0068	0,0051
Autapse GABA	-	0,007

518 *values based on^{19,27,44,45,47,55}

519

520 **References:**

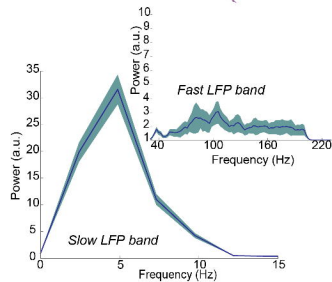
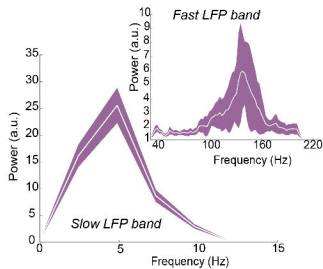
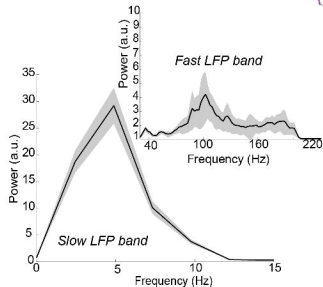
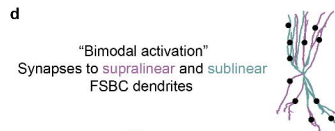
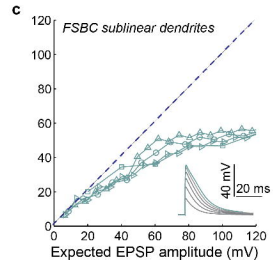
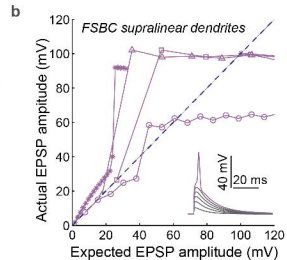
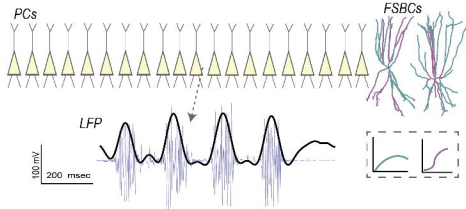
- 521 1. Buzsáki, G. & Draguhn, A. Neuronal Oscillations in Cortical Networks. *Science* (80-.).
522 **304**, 1926–1929 (2004).
- 523 2. Jackson, J. & Skinner, F. K. Hippocampus, Theta, Gamma, and Cross-Frequency
524 Coupling. in *Encyclopedia of Computational Neuroscience* 1–11 (Springer New York,
525 2018). doi:10.1007/978-1-4614-7320-6_30-2.
- 526 3. Lisman, J. E. & Jensen, O. The Theta-Gamma Neural Code. *Neuron* **77**, 1002–1016
527 (2013).
- 528 4. Griffiths, B. J. & Jensen, O. Gamma oscillations and episodic memory. *Trends*
529 *Neurosci.* **46**, 832–846 (2023).
- 530 5. Tort, A. B. L., Scheffer-Teixeira, R., Souza, B. C., Draguhn, A. & Brankačk, J. Theta-
531 associated high-frequency oscillations (110–160Hz) in the hippocampus and
532 neocortex. *Prog. Neurobiol.* **100**, 1–14 (2013).
- 533 6. Buzsáki, G. & Wang, X.-J. Mechanisms of Gamma Oscillations. *Annu. Rev. Neurosci.*
534 **35**, 203–225 (2012).
- 535 7. Buzsáki, G. Two-stage model of memory trace formation: A role for “noisy” brain
536 states. *Neuroscience* **31**, 551–570 (1989).
- 537 8. Jackson, J., Goutagny, R. & Williams, S. Fast and Slow Gamma Rhythms Are
538 Intrinsically and Independently Generated in the Subiculum. *J. Neurosci.* **31**, 12104–
539 12117 (2011).
- 540 9. Zhang, X. *et al.* Impaired theta-gamma coupling in APP-deficient mice. *Sci. Rep.* **6**,
541 21948 (2016).
- 542 10. Wulff, P. *et al.* Hippocampal theta rhythm and its coupling with gamma oscillations
543 require fast inhibition onto parvalbumin-positive interneurons. *Proc. Natl. Acad. Sci.*
544 **106**, 3561–3566 (2009).
- 545 11. Schomburg, E. W. *et al.* Theta Phase Segregation of Input-Specific Gamma Patterns
546 in Entorhinal-Hippocampal Networks. *Neuron* **84**, 470–485 (2014).
- 547 12. Tzilivaki, A. *et al.* Hippocampal GABAergic interneurons and memory. *Neuron* **111**,
548 3154–3175 (2023).
- 549 13. Topolnik, L. & Tamboli, S. The role of inhibitory circuits in hippocampal memory
550 processing. *Nat. Rev. Neurosci.* **23**, 476–492 (2022).
- 551 14. Cardin, J. A. *et al.* Driving fast-spiking cells induces gamma rhythm and controls
552 sensory responses. *Nature* **459**, 663–667 (2009).
- 553 15. Pelkey, K. A. *et al.* Hippocampal gabaergic inhibitory interneurons. *Physiol. Rev.* **97**,
554 1619–1747 (2017).
- 555 16. Allen, K. & Monyer, H. Interneuron control of hippocampal oscillations. *Curr. Opin.*
556 *Neurobiol.* **31**, 81–87 (2015).

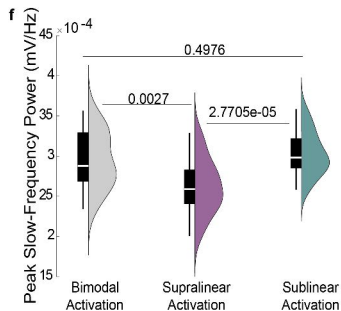
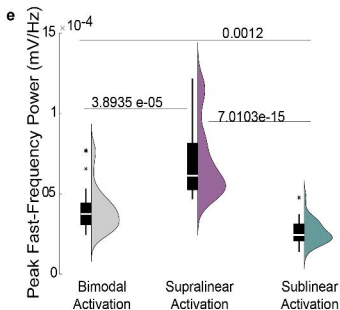
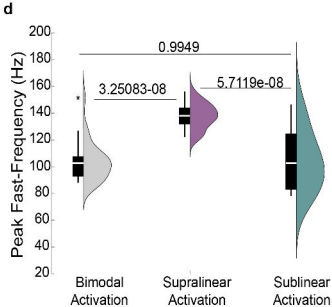
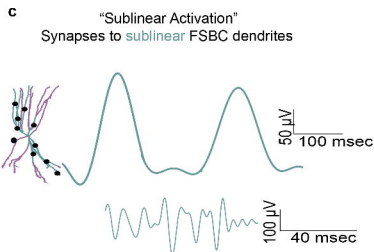
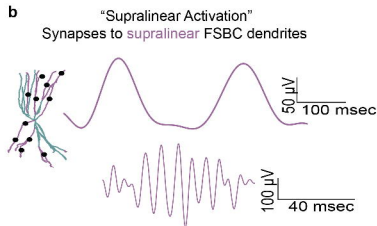
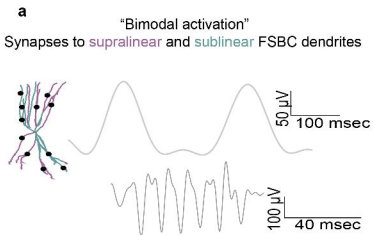
- 557 17. Lucas, E. K. & Clem, R. L. GABAergic interneurons: The orchestra or the conductor in
558 fear learning and memory? *Brain Res. Bull.* **141**, 13–19 (2018).
- 559 18. Tzilivaki, A., Kastellakis, G., Schmitz, D. & Poirazi, P. GABAergic Interneurons with
560 Nonlinear Dendrites: From Neuronal Computations to Memory Engrams.
561 *Neuroscience* **489**, 34–43 (2022).
- 562 19. Tzilivaki, A., Kastellakis, G. & Poirazi, P. Challenging the point neuron dogma: FS
563 basket cells as 2-stage nonlinear integrators. *Nat. Commun.* **10**, 3664 (2019).
- 564 20. Chiovini, B. *et al.* Dendritic Spikes Induce Ripples in Parvalbumin Interneurons during
565 Hippocampal Sharp Waves. *Neuron* **82**, 908–924 (2014).
- 566 21. Cornford, J. H. *et al.* Dendritic NMDA receptors in parvalbumin neurons enable strong
567 and stable neuronal assemblies. *Elife* **8**, (2019).
- 568 22. Hu, H. & Vervaeke, K. Synaptic Integration in Cortical Inhibitory Neuron Dendrites.
569 *Neuroscience* **368**, 115–131 (2018).
- 570 23. Katona, G. *et al.* Roller Coaster Scanning reveals spontaneous triggering of dendritic
571 spikes in CA1 interneurons. *Proc. Natl. Acad. Sci. U. S. A.* **108**, 2148–2153 (2011).
- 572 24. Cornford, J. H. *et al.* Dendritic NMDA receptors in parvalbumin neurons enable strong
573 and stable neuronal assemblies. *Elife* **8**, (2019).
- 574 25. Chamberland, S. & Topolnik, L. Inhibitory control of hippocampal inhibitory neurons.
575 *Front. Neurosci.* **6**, 1–13 (2012).
- 576 26. Klausberger, T. & Somogyi, P. Neuronal Diversity and Temporal Dynamics: The Unity
577 of Hippocampal Circuit Operations. *Science (80-.)*. **321**, (2008).
- 578 27. Hadler, M. D., Tzilivaki, A., Schmitz, D., Alle, H. & Geiger, J. R. P. Gamma oscillation
579 plasticity is mediated via parvalbumin interneurons. *Sci. Adv.* **10**, (2024).
- 580 28. Park, K. *et al.* Optogenetic activation of parvalbumin and somatostatin interneurons
581 selectively restores theta-nested gamma oscillations and oscillation-induced spike
582 timing-dependent long-term potentiation impaired by amyloid β oligomers. *BMC Biol.*
583 **18**, 7 (2020).
- 584 29. Turi, G. F. *et al.* Vasoactive Intestinal Polypeptide-Expressing Interneurons in the
585 Hippocampus Support Goal-Oriented Spatial Learning. *Neuron* **101**, 1150-1165.e8
586 (2019).
- 587 30. Kastellakis, G., Cai, D. J., Mednick, S. C., Silva, A. J. & Poirazi, P. Synaptic clustering
588 within dendrites: An emerging theory of memory formation. *Prog. Neurobiol.* **126**, 19–
589 35 (2015).
- 590 31. Hu, H., Gan, J. & Jonas, P. Interneurons. Fast-spiking, parvalbumin⁺ GABAergic
591 interneurons: from cellular design to microcircuit function. *Science* **345**, 1255263
592 (2014).
- 593 32. Tort, A. B. L., Komorowski, R., Eichenbaum, H. & Kopell, N. Measuring Phase-
594 Amplitude Coupling Between Neuronal Oscillations of Different Frequencies. *J.*
595 *Neurophysiol.* **104**, 1195–1210 (2010).
- 596 33. Scheffzük, C. *et al.* Selective Coupling between Theta Phase and Neocortical Fast
597 Gamma Oscillations during REM-Sleep in Mice. *PLoS One* **6**, e28489 (2011).
- 598 34. Scheffer-Teixeira, R. *et al.* Theta Phase Modulates Multiple Layer-Specific
599 Oscillations in the CA1 Region. *Cereb. Cortex* **22**, 2404–2414 (2012).

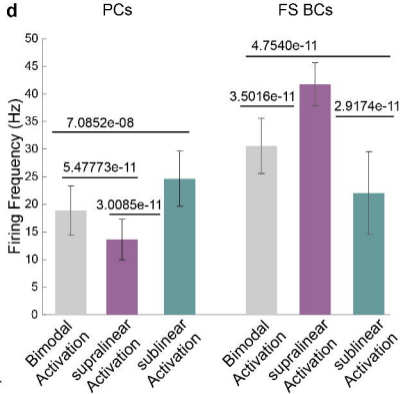
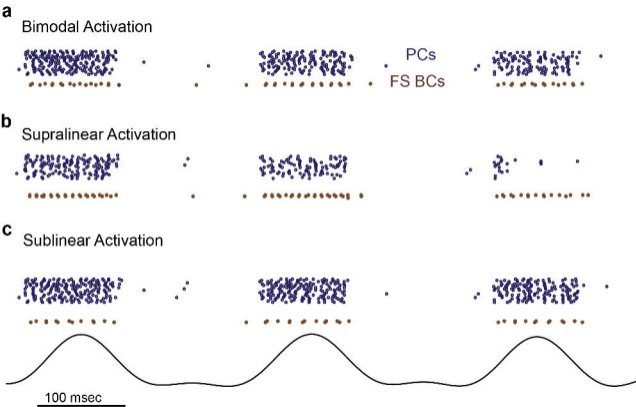
- 600 35. Belluscio, M. A., Mizuseki, K., Schmidt, R., Kempster, R. & Buzsáki, G. Cross-
601 Frequency Phase–Phase Coupling between Theta and Gamma Oscillations in the
602 Hippocampus. *J. Neurosci.* **32**, 423–435 (2012).
- 603 36. Canolty, R. T. *et al.* High Gamma Power Is Phase-Locked to Theta Oscillations in
604 Human Neocortex. *Science (80-.)*. **313**, 1626–1628 (2006).
- 605 37. Judák, L. *et al.* Sharp-wave ripple doublets induce complex dendritic spikes in
606 parvalbumin interneurons in vivo. *Nat. Commun.* **13**, 6715 (2022).
- 607 38. Kriener, B., Hu, H. & Vervaeke, K. Parvalbumin interneuron dendrites enhance
608 gamma oscillations. *Cell Rep.* **39**, 110948 (2022).
- 609 39. Liao, Z. *et al.* Functional architecture of intracellular oscillations in hippocampal
610 dendrites. *bioRxiv* 2024.02.12.579750 (2024).
- 611 40. Fernández-Ruiz, A. *et al.* Gamma rhythm communication between entorhinal cortex
612 and dentate gyrus neuronal assemblies. *Science (80-.)*. **372**, (2021).
- 613 41. Hines, M. L. & Carnevale, N. T. The NEURON Simulation Environment. *Neural*
614 *Comput.* **9**, 1179–1209 (1997).
- 615 42. Tukker, J. J., Fuentealba, P., Hartwich, K., Somogyi, P. & Klausberger, T. Cell type-
616 specific tuning of hippocampal interneuron firing during gamma oscillations in vivo. *J.*
617 *Neurosci.* **27**, 8184–8189 (2007).
- 618 43. Sun, Q. *et al.* Proximodistal Heterogeneity of Hippocampal CA3 Pyramidal Neuron
619 Intrinsic Properties, Connectivity, and Reactivation during Memory Recall. *Neuron* **95**,
620 656-672.e3 (2017).
- 621 44. Banke, T. G. & McBain, C. J. GABAergic Input onto CA3 Hippocampal Interneurons
622 Remains Shunting throughout Development. *J. Neurosci.* **26**, 11720–11725 (2006).
- 623 45. Fukushima, F. *et al.* Ablation of NMDA Receptors Enhances the Excitability of
624 Hippocampal CA3 Neurons. *PLoS One* **4**, e3993 (2009).
- 625 46. Kohus, Z. *et al.* Properties and dynamics of inhibitory synaptic communication within
626 the CA3 microcircuits of pyramidal cells and interneurons expressing parvalbumin or
627 cholecystokinin. *J. Physiol.* **594**, 3745–3774 (2016).
- 628 47. Wang, H.-X. & Gao, W.-J. Cell type-specific development of NMDA receptors in the
629 interneurons of rat prefrontal cortex. *Neuropsychopharmacology* **34**, 2028–40 (2009).
- 630 48. Turi, G. F. *et al.* Vasoactive Intestinal Polypeptide-Expressing Interneurons in the
631 Hippocampus Support Goal-Oriented Spatial Learning. *Neuron* **101**, 1150-1165.e8
632 (2019).
- 633 49. Vladimirov, N., Tu, Y. & Traub, R. D. Synaptic gating at axonal branches, and
634 sharp-wave ripples with replay: a simulation study. *Eur. J. Neurosci.* **38**, 3435–3447
635 (2013).
- 636 50. Tort, A. B. L. *et al.* Dynamic cross-frequency couplings of local field potential
637 oscillations in rat striatum and hippocampus during performance of a T-maze task.
638 *Proc. Natl. Acad. Sci.* **105**, 20517–20522 (2008).
- 639 51. Goldberg, J. H., Yuste, R. & Tamas, G. Ca²⁺ imaging of mouse neocortical
640 interneurone dendrites: contribution of Ca²⁺-permeable AMPA and NMDA receptors
641 to subthreshold Ca²⁺dynamics. *J. Physiol.* **551**, 67–78 (2003).
- 642 52. Goldberg, J. H. & Yuste, R. Space matters: Local and global dendritic Ca²⁺
643 compartmentalization in cortical interneurons. *Trends Neurosci.* **28**, 158–167 (2005).

- 644 53. Nörenberg, A., Hu, H., Vida, I., Bartos, M. & Jonas, P. Distinct nonuniform cable
645 properties optimize rapid and efficient activation of fast-spiking GABAergic
646 interneurons. *Proc. Natl. Acad. Sci. U. S. A.* **107**, 894–9 (2010).
- 647 54. Bacci, A., Rudolph, U., Huguenard, J. R. & Prince, D. A. Cellular/Molecular Major
648 Differences in Inhibitory Synaptic Transmission onto Two Neocortical Interneuron
649 Subclasses.
- 650 55. Kohus, Z. *et al.* Properties and dynamics of inhibitory synaptic communication within
651 the CA3 microcircuits of pyramidal cells and interneurons expressing parvalbumin or
652 cholecystokinin. *J. Physiol.* **594**, 3745–3774 (2016).
- 653

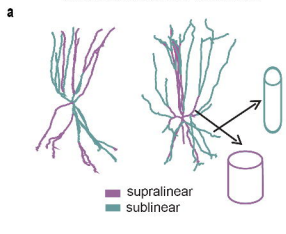
a *Microcircuit model of hippocampal oscillations*



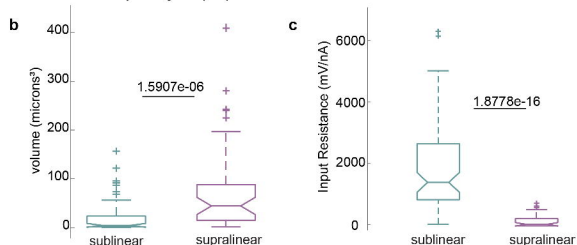




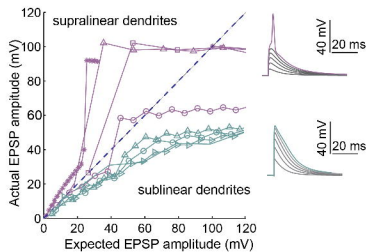
Hippocampal FS BCs with bimodal nonlinear dendrites



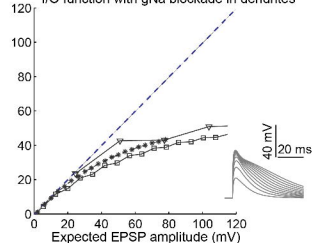
Morphological properties nonlinear dendrites in FS BCs trees



d Control I/O functions



e I/O function with gNa blockade in dendrites



Sublinear and Supralinear forward propagation

